



Contributions to the development of an axisymmetric SAW motor with a stator made from non-piezoelectric material

Richard Günther*, René Richter, Jens Lienig

Institute of Electromechanical and Electronic Design, Dresden University of Technology, Germany

ARTICLE INFO

Article history:

Received 13 December 2017
 Received in revised form 12 March 2019
 Accepted 18 April 2019
 Available online 22 April 2019

Keywords:

Ultrasonic motor
 SAW actuators
 Axisymmetric
 Cylindric
 Rayleigh waves
 Piezoelectric
 PZT

ABSTRACT

Surface acoustic wave (SAW) motors offer great potential due to their high blocking forces, high positioning accuracy and simple design. As established SAW motors have a plane stator made by piezoelectric single crystals, designers have nearly no influence on changing material properties like the friction coefficient or brittleness. Furthermore, the efficiency decreases with rising travel length, caused by components of the SAW passing the slider. This article presents the theory of Rayleigh waves on cylindric rods in axial direction of propagation. Based on this, a new axisymmetric motor structure with a stator made from non-piezoelectric base material, which could avoid the problems mentioned above, was analytically characterized. Furthermore, a prototype of a plane SAW motor made from non-piezoelectric steel is presented. SAW were generated by small piezoelectric units made from lead zirconate titanate (PZT). At the working frequency of 3.85 MHz a SAW with an efficiency of 17% was generated. An idling speed of 29 mm s⁻¹ and a blocking force of 0.19 N were measured therewith. Finally, we present a SAW generation by thick film technology. This technology allows the manufacture of piezoelectric units on cylindric rods that are necessary for the mentioned axisymmetric SAW motors. Our prototypes are compared to numeric models.

© 2019 Elsevier B.V. All rights reserved.

1. Introduction

Caused by improvements of electronic controlling, more and more small independent actuators will be placed in a wide variety of products. Automotive engineering is a good example for this trend. Currently, an average car contains 120 or more electric motors aiding with different driving assistants and comfort features [1]. The common motor type is the electrodynamic one. It is cheap and highly efficient. However, caused by the needed coils it is hard to miniaturize the electromagnetic motor. When a linear motion with low speed or self locking effect is required, it is often realized by an electric motor combined with a screw driver. Such actuators have a complex design and an indirect force transmission.

A lot of ultrasonic motors enable linear motion with such requirements, having a relative simple design. For example [2–6] present ultrasonic motors, which use several acoustic modes to generate a directed motion of the stator's contact surface. An ultrasonic motor with a cylindric slider which can be rotated and translated as well is shown by [7]. The stator is a cube with a hole

that encases the slider. Depending on the used resonance mode, the directed motion of the contact surface inside the hole moves the slider in the same way as mentioned before. Shigematsu [8] presents an ultrasonic linear motor using surface acoustic waves (SAW). The stator is a substrate made from LiNbO₃ with a thickness of 1 mm. Inter-digital transducer are used to generate surface acoustic waves on the stator. A slider is pressed onto the substrate as shown in Fig. 1a. Thus, it can be moved by the SAW. The surface of the slider is patterned to increase the motor power. It is supposed that the reduction of contact area, in other words the increase of contact pressure, is required to avoid a film of air between stator and slider [9]. A small wavelength in accordance with a high frequency compared to common ultrasonic motors is typical for these SAW motors. This supports a better miniaturization and a higher power density of SAW motors [10]. Furthermore, a sub-nanometer positioning seems to be possible [8]. As the friction coefficient between LiNbO₃ and silicon is about 0.18 [11], preload must be about five times higher than the output force. This preload must be applied by a further configuration. Apart from that, the stator is made of brittle and expensive material.

If the stator is made of non-piezoelectric material, a larger variety of materials would be available. Thus, a lower price for the stator material, a tougher stator and a higher friction coefficient would be

* Corresponding author.

E-mail address: richard.guenther@tu-dresden.de (R. Günther).

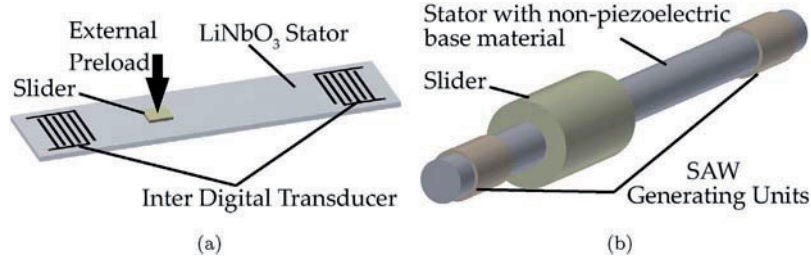


Fig. 1. (a) Fundamental structure of the common plane SAW motor with a stator made from piezoelectric LiNbO₃ presented in [8]; SAW are generated by an inter-digital transducer (IDT); (b) fundamental structure of the proposed axisymmetric SAW motor with non-piezoelectric stator base material and separate SAW generating units; in contrast to the common plane SAW motor, the slider would automatically be pressed onto the stator and proportions of the SAW cannot pass the slider at its side.



Fig. 2. Orientation of a cylinder in a cylindrical coordinate system that is used to derive Rayleigh waves on its surface.

possible. In that case, a small piezoelectric unit creates the SAW on the non-piezoelectric stator base material as shown in Fig. 1b. If the stator is axisymmetric, proportions of the SAW cannot pass the slider at its side and the slider would automatically be pressed onto the stator. As no further configuration for preload generation is needed, a simpler design is possible.

The contribution of this paper is an extension of the theory of Rayleigh waves applied to cylindrical rods in axial direction of propagation, the resulting analytical quantification of these SAW and the analytical characterization of appropriate axisymmetric SAW motors. Furthermore, we present a plane SAW motor with a stator made from non-piezoelectric material. In addition, we generated SAW on a plane non-piezoelectric material by an actuator unit which is made by use of thick-film technology. This technology allows a SAW excitation on cylindrical rods too, and enables the manufacture of such axisymmetric stators.

2. Theory of Rayleigh waves on axisymmetric rods in axial direction of propagation

As the behavior of Rayleigh waves on cylinders differs from the behavior on a plane half space, it is useful to describe Rayleigh waves on axisymmetric rods to enable a characterization of the proposed motor. Thus, within this Section we describe the theory of Rayleigh waves in cylindrical coordinates in axial direction of propagation. This approach is adopted from the derivation of plane harmonic Rayleigh waves, as documented by Viktorov [12]. Within this derivation the indices for the radial, angular and axial vector components are r , θ and z , respectively. The indices for radial, angular and axial stress and strain components are rr , $\theta\theta$ and zz , respectively. For differentiation, the Leibniz's notation is used.

We make the following assumptions: the Rayleigh waves travel on an ideal infinitely long cylindrical rod of isotropic material, surrounded by vacuum. According to Fig. 2 the mid of the cylindrical rod is located on the z -axis. Its radius is R_0 . Considering the axial symmetry, we can define the displacement of the solid \vec{u} , the strain $\vec{\epsilon}$ and the stress $\vec{\sigma}$ of the material as follows [13]:

$$\vec{u} = \begin{pmatrix} u_r(r, z, t) \\ 0 \\ u_z(r, z, t) \end{pmatrix}, \quad (1)$$

$$\vec{\epsilon} = \begin{pmatrix} \epsilon_{rr}(r, z, t) \\ \epsilon_{\theta\theta}(r, z, t) \\ \epsilon_{zz}(r, z, t) \\ \gamma_{rz}(r, z, t) \end{pmatrix} = \begin{pmatrix} \frac{\partial u_r}{\partial r} \\ \frac{u_r}{r} \\ \frac{\partial u_z}{\partial z} \\ \left(\frac{\partial u_r}{\partial z} + \frac{\partial u_z}{\partial r} \right) \end{pmatrix}, \quad (2)$$

$$\vec{\sigma} = \begin{pmatrix} \sigma_{rr}(r, z, t) \\ \sigma_{\theta\theta}(r, z, t) \\ \sigma_{zz}(r, z, t) \\ \sigma_{rz}(r, z, t) \end{pmatrix} = \begin{pmatrix} 2\mu \frac{\partial u_r}{\partial r} + \lambda \operatorname{div} \vec{u} \\ 2\mu \frac{u_r}{r} + \lambda \operatorname{div} \vec{u} \\ 2\mu \frac{\partial u_z}{\partial z} + \lambda \operatorname{div} \vec{u} \\ \mu \left(\frac{\partial u_r}{\partial z} + \frac{\partial u_z}{\partial r} \right) \end{pmatrix}. \quad (3)$$

t is the time, r and z are the radial and axial coordinates of the cylindrical coordinate system, respectively, used in this derivation. γ_{rz} and σ_{rz} are the engineering shear strain and shear stress in r - z -plane, respectively, μ and λ are the Lamé parameters. Furthermore, the stresses σ_{rr} and σ_{rz} on the cylinder's surface must be zero:

$$\sigma_{rr}(R_0, z, t) = 0, \quad (4)$$

$$\sigma_{rz}(R_0, z, t) = 0. \quad (5)$$

The starting point of the derivation is the general three dimensional wave equation for isotropic materials and the superposition approach for longitudinal and transversal waves:

$$\mu \Delta \vec{u} + (\mu + \lambda) \operatorname{grad} \operatorname{div} \vec{u} = \rho_0 \frac{\partial^2 \vec{u}}{\partial t^2}, \quad (6)$$

$$\begin{aligned} \vec{u} &= \vec{u}_L + \vec{u}_T = \operatorname{grad} \Phi(r, z, t) + \operatorname{rot} \vec{\Psi}(r, z, t) \\ &= \begin{pmatrix} \frac{\partial \phi(r, z, t)}{\partial r} \\ 0 \\ \frac{\partial \Phi(r, z, t)}{\partial z} \end{pmatrix} + \begin{pmatrix} -\frac{\partial h(r, z, t)}{\partial z} \\ 0 \\ \frac{1}{r} \frac{\partial (r \cdot h(r, z, t))}{\partial r} \end{pmatrix}, \end{aligned} \quad (7)$$

$$\text{with } \vec{\Psi}(r, z, t) = \begin{pmatrix} 0 \\ h(r, z, t) \\ 0 \end{pmatrix}.$$

ρ_0 is the density of the solid material, \vec{u}_L and \vec{u}_T are the displacement vectors of the longitudinal and transversal wave components, respectively, $\Phi(r, z, t)$ is an auxiliary scalar potential and $\vec{\Psi}(r, z, t)$ is an auxiliary vector potential. Its sole non-zero component is the azimuth that is equivalent to the auxiliary scalar potential

$h(r, z, t)$. The longitudinal component of the wave equation appears as follows:

$$\mu \Delta \text{grad } \Phi + (\mu + \lambda) \text{grad } \text{div grad } \Phi = \rho_0 \frac{\partial^2 \text{grad } \Phi}{\partial t^2}, \tag{8}$$

$$\frac{\partial}{r \partial r} \left(\frac{r \partial \Phi}{\partial r} \right) + \frac{\partial^2 \Phi}{\partial z^2} + k_L^2 \Phi = 0, \text{ with } k_L = \omega \sqrt{\frac{\rho_0}{2\mu + \lambda}}$$

k_L is the wavenumber of the longitudinal wave. As we consider just the harmonic case, $\partial^2/\partial t^2$ is replaced by $-\omega^2$, whereby $\omega = 2\pi f$ is the angular velocity as a function of the frequency f . We can present the transversal component in a similar fashion:

$$\mu(\text{grad div rot } \bar{\Psi} - \text{rot rot rot } \bar{\Psi}) + (\mu + \lambda) \text{grad div rot } \bar{\Psi} = \rho_0 \frac{\partial^2 \text{rot } \bar{\Psi}}{\partial t^2}. \tag{9}$$

As $\text{div rot } \bar{\Psi} = 0$ we can simplify the equation of the transversal wave:

$$-\text{rot rot} \begin{pmatrix} -\frac{\partial h}{\partial z} \\ 0 \\ \frac{1}{r} \frac{\partial(r \cdot h)}{\partial r} \end{pmatrix} + \frac{\rho_0 \omega^2}{\mu} \begin{pmatrix} -\frac{\partial h}{\partial z} \\ 0 \\ \frac{1}{r} \frac{\partial(r \cdot h)}{\partial r} \end{pmatrix} = 0,$$

$$\begin{pmatrix} \frac{\partial h}{r^2 \partial z} - \frac{\partial^3 h}{\partial r^2 \partial z} - \frac{\partial^3 h}{\partial z^3} - \frac{\partial^2 h}{r \partial r \partial z} \\ 0 \\ \frac{\partial^3 h}{\partial r \partial z^2} + \frac{\partial^2 h}{r \partial z^2} + \frac{2 \partial^2 h}{r \partial r^2} - \frac{\partial h}{r^2 \partial r} + \frac{h}{r^3} + \frac{\partial^3 h}{\partial r^3} \end{pmatrix} \tag{10}$$

$$+ \frac{\rho_0 \omega^2}{\mu} \begin{pmatrix} -\frac{\partial h}{\partial z} \\ 0 \\ \frac{1}{r} \frac{\partial(r \cdot h)}{\partial r} \end{pmatrix} = 0.$$

Eq. (10) has a radial, an angular and an axial component. Each component can be viewed as a separate equation. So we see that all terms of the azimuth equation are zero. The radial and the axial equations are as follows:

$$\Delta h - \frac{h}{r^2} + k_T^2 h = 0, \text{ with } k_T = \omega \sqrt{\frac{\rho_0}{\mu}}. \tag{11}$$

k_T is the wavenumber of the transversal wave. Thus, we can assume $\bar{\Psi}$ as a scalar potential $\Psi = h$. Then we can write the longitudinal and transversal wave equations as:

$$\frac{\partial}{r \partial r} \left(\frac{r \partial \Phi}{\partial r} \right) + \frac{\partial^2 \Phi}{\partial z^2} + k_L^2 \Phi = 0, \tag{12}$$

$$\frac{\partial}{r \partial r} \left(\frac{r \partial \Psi}{\partial r} \right) + \frac{\partial^2 \Psi}{\partial z^2} - \frac{\Psi}{r^2} + k_T^2 \Psi = 0.$$

As the SAW is a harmonic wave, we can describe Φ and Ψ as:

$$\Phi = X(r) e^{i(k_A z - \omega t)}, \tag{13}$$

$$\Psi = Y(r) e^{i(k_A z - \omega t)}.$$

k_A is the wavenumber of the axisymmetric Rayleigh wave. The unknown functions $X(r)$ and $Y(r)$ describe the influence of the radius

containing the decrease of the intensity of the wave for decreasing radii. Substitution of Eq. (13) into Eq. (12) yields to

$$\frac{\partial^2 X}{\partial r^2} + \frac{\partial X}{r \partial r} + X(k_L^2 - k_A^2) = 0. \tag{14}$$

$$\frac{\partial^2 Y}{\partial r^2} + \frac{\partial Y}{r \partial r} - \frac{Y}{r^2} + Y(k_T^2 - k_A^2) = 0.$$

The solutions of these differential equations are:

$$X = C_1 J_0(iq_A r) + C_2 Y_0(iq_A r),$$

$$Y = C_3 I_1(is_A r) + C_4 Y_1(is_A r), \tag{15}$$

with $q_A^2 = k_A^2 - k_L^2$, $s_A^2 = k_A^2 - k_T^2$.

C_1 , C_2 , C_3 and C_4 are unknown constants so far. J_0 and Y_0 are the Bessel functions of the first and second kind, respectively, and of order zero. J_1 and Y_1 are the Bessel functions of the first and second kind, respectively, but of order one. As $u_z(0, z, t) = 0$ for axisymmetric problems, Eq. (15) can be simplified as follows:

$$X = C_1 I_0(q_A r), \tag{16}$$

$$Y = -iC_3 I_1(s_A r) = C_3 I_1(s_A r).$$

I_0 and I_1 are the modified Bessel functions of the first kind and of order zero and one, respectively. C_3 is a further constant that will be determined later on. So the auxiliary potentials Φ and Ψ can be described as

$$\Phi = C_1 I_0(q_A r) e^{i(k_A z - \omega t)}, \tag{17}$$

$$\Psi = C_3 I_1(s_A r) e^{i(k_A z - \omega t)}.$$

With Ψ as scalar potential, the axial and radial displacements in Eq. (7) have the form

$$u_r = \frac{\partial \Phi}{\partial r} - \frac{\partial \Psi}{\partial z}, \tag{18}$$

$$u_z = \frac{\partial \Phi}{\partial z} + \frac{\partial(r\Psi)}{r \partial r}$$

and can be substituted into the stress tensor (3):

$$\bar{\sigma} = \begin{pmatrix} \lambda \left(\frac{\partial \Phi}{r \partial r} + \frac{\partial^2 \Phi}{\partial r^2} + \frac{\partial^2 \Phi}{\partial z^2} \right) + 2\mu \left(\frac{\partial^2 \Phi}{\partial r^2} - \frac{\partial^2 \Psi}{\partial r \partial z} \right) \\ \lambda \left(\frac{\partial \Phi}{r \partial r} + \frac{\partial^2 \Phi}{\partial r^2} + \frac{\partial^2 \Phi}{\partial z^2} \right) + 2\mu \left(\frac{\partial \Phi}{r \partial r} - \frac{\partial \Psi}{r \partial z} \right) \\ \lambda \left(\frac{\partial \Phi}{r \partial r} + \frac{\partial^2 \Phi}{\partial r^2} + \frac{\partial^2 \Phi}{\partial z^2} \right) + 2\mu \left(\frac{\partial^2 \Phi}{\partial z^2} + \frac{\partial \Psi}{r \partial z} + \frac{\partial^2 \Psi}{\partial r \partial z} \right) \\ \mu \left(2 \frac{\partial^2 \Phi}{\partial r \partial z} + \frac{\partial^2 \Psi}{\partial r^2} - \frac{\partial^2 \Psi}{\partial z^2} + \frac{\partial \Psi}{r \partial r} - \frac{\Psi}{r^2} \right) \end{pmatrix}. \tag{19}$$

In order to determine the constant C_3 , we can substitute Eqs. (19) and (17) into the constraint (5):

$$\mu \left(2 \frac{\partial^2 \Phi(R_0, z, t)}{\partial r \partial z} + \frac{\partial^2 \Psi(R_0, z, t)}{\partial r^2} - \frac{\partial^2 \Psi(R_0, z, t)}{\partial z^2} \right) + \mu \left(\frac{\partial \Psi(R_0, z, t)}{r \partial r} - \frac{\Psi(R_0, z, t)}{r^2} \right) = 0, \tag{20}$$

$$C_3 = C_1 \frac{-2iq_A k_A I_1(q_A R_0)}{k_A^2 + s_A^2 I_1(s_A R_0)}$$

The constant C_1 can be replaced by a negated amplitude a , which describes the intensity of the SAW:

$$C_1 = -a. \tag{21}$$

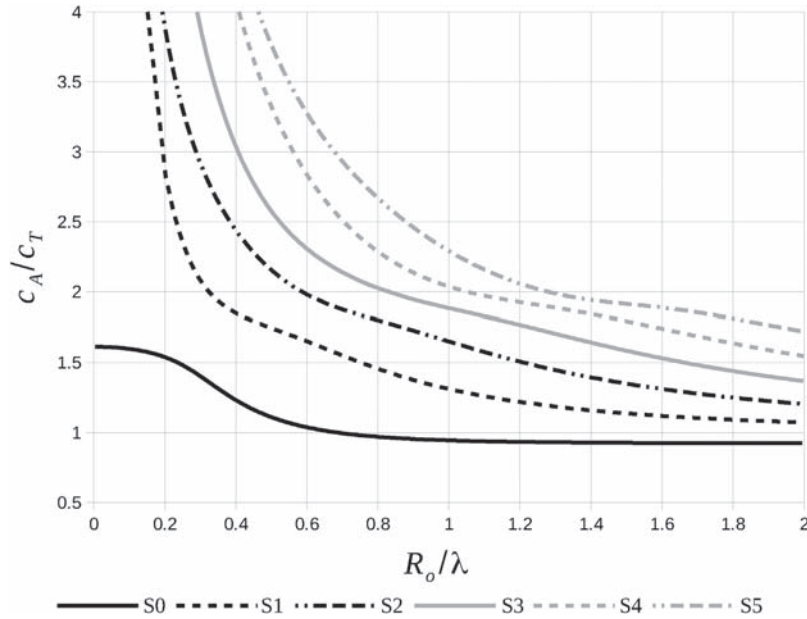


Fig. 3. Dispersion curves of axisymmetric waves in rods: wave velocity of the six first modes S0–S5 normalized to shear velocity c_T as a function of the rod radius normalized to wavelength; $\nu=0.3$.

Thus, the auxiliary potentials Φ and Ψ can be described as

$$\begin{aligned} \Phi &= -aI_0(q_A r)e^{i(k_A z - \omega t)}, \\ \Psi &= ia \frac{2q_A k_A}{k_A^2 + s_A^2} \frac{I_1(q_A R_o)}{I_1(s_A R_o)} I_1(s_A r) e^{i(k_A z - \omega t)}. \end{aligned} \tag{22}$$

Substituting Eq. (22) into Eq. (18) leads to a definition of the motion of the solid material:

$$\begin{aligned} u_r &= \Re \left(\frac{\partial \Phi}{\partial r} - \frac{\partial \Psi}{\partial z} \right), \\ u_z &= \Re \left(\frac{\partial \Phi}{\partial z} + \frac{\Psi}{r} + \frac{\partial \Psi}{\partial r} \right), \\ u_r &= aq_A \left(\frac{2k_A^2}{k_A^2 + s_A^2} \frac{I_1(q_A R_o)}{I_1(s_A R_o)} I_1(s_A r) - I_1(q_A r) \right) \cdot \cos(k_A z - \omega t), \\ u_z &= ak_A \left(I_0(q_A r) - \frac{2q_A s_A}{k_A^2 + s_A^2} \frac{I_1(q_A R_o)}{I_1(s_A R_o)} I_0(s_A r) \right) \cdot \sin(k_A z - \omega t). \end{aligned} \tag{23}$$

\Re is the real part operator.

At this point only the wavenumber of the axisymmetric Rayleigh wave k_A is still unknown. It can be determined by substituting the stress tensor (19) with the auxiliary potentials (17) into the boundary condition (4):

$$\begin{aligned} \lambda \left(\frac{\partial \Phi(R_o, z, t)}{R_o \partial r} + \frac{\partial^2 \Phi(R_o, z, t)}{\partial r^2} + \frac{\partial^2 \Phi(R_o, z, t)}{\partial z^2} \right) \\ + 2\mu \left(\frac{\partial^2 \Phi(R_o, z, t)}{\partial r^2} - \frac{\partial^2 \Psi(R_o, z, t)}{\partial r \partial z} \right) = 0, \\ C_1(R_o I_0(q_A R_o))((\lambda + 2\mu)q_A^2 - \lambda k_A^2) - 2\mu q_A I_1(q_A R_o) \\ + 2\mu i k_A C_3(I_1(s_A R_o) - s_A R_o I_0(s_A R_o)) = 0. \end{aligned} \tag{24}$$

By substituting the constants C_1 (21) and C_3 (20) into Eq. (24), we get the following equation:

$$\frac{2s_A}{k_A^2 + s_A^2} \left(k_A^2 R_o \frac{I_0(s_A R_o)}{I_1(s_A R_o)} + s_A \right) = \frac{R_o(k_A^2 + s_A^2)}{2q_A} \frac{I_0(q_A R_o)}{I_1(q_A R_o)} + 1. \tag{25}$$

Eq. (25) must be solved numerically to determine the wavenumber k_A of the axisymmetric Rayleigh wave. However, the following connectedness can be determined:

$$k_A = \frac{k_T}{\nu \left(R_o f \sqrt{\frac{\rho_0}{D}}, \nu \right)}. \tag{26}$$

ν is the ratio of wavenumber for transversal to axisymmetric Rayleigh waves, ν is the Poisson's ratio and D is the Young's modulus. Eq. (25) can have more than one solution for a specific frequency. This implies, that several wave modes are possible. Fig. 3 presents the wave velocity $c_A = \omega/k_A$ normalized to the velocity of transversal waves c_T for several modes. This normalized velocity equals to ν and depends on the ratio of rod radius to wavelength

$$\Lambda_A = \frac{2\pi}{k_A}. \tag{27}$$

That means, axisymmetric waves in rods are dispersive. The curves, presented in Fig. 3 resemble the dispersion curves of Lamb waves. However, due to axisymmetry only the symmetric modes exist. The S0 mode is the axisymmetric Rayleigh mode, we want to use. For small rod radius to wavelength ratios its velocity approximates to that of longitudinal waves, neglecting transversal stress. The higher the rod radius to wavelength ratio, the more ν approximates $(0.87 + 1.12\nu)/(1 + \nu)$, which is mentioned for plane Rayleigh waves [12]. Fig. 4 presents the maximum radial and axial displacements $\hat{u}_r(r)$ and $\hat{u}_z(r)$, respectively, normalized to the maximum radial displacement at the outer radius $\hat{u}_r(R_o)$. They are plotted as a function of the radius normalized to rod radius for several ratios of rod radius to wavelength. This figure visualizes the mentioned behavior. For small rod radius to wavelength ratios the displacements approximates the longitudinal wave. With rising relative radius the relevant motion concentrates at outer region and the displacements approximates that ones, described for plane Rayleigh waves.

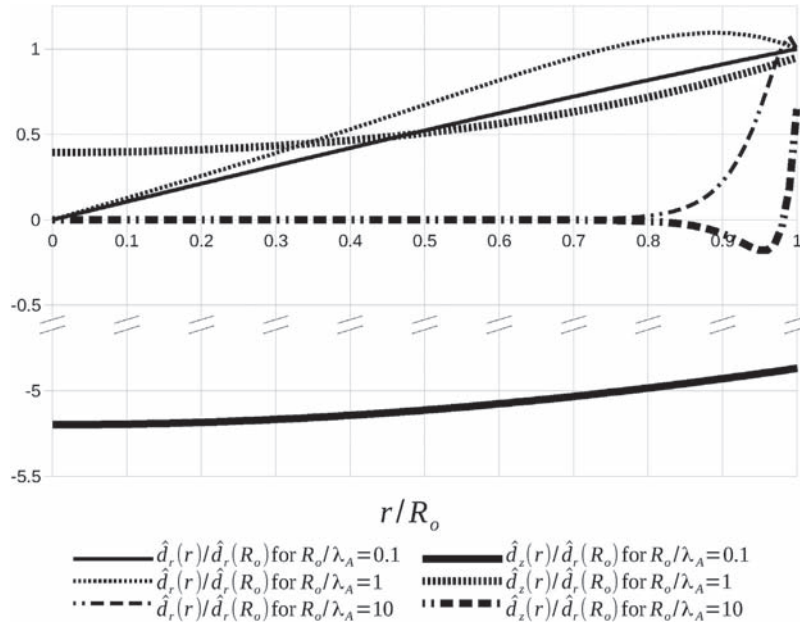


Fig. 4. Maximum radial and axial displacements normalized to maximum radial displacement at the outer radius as a function of the radius normalized to rod radius for ratios of rod radius to wavelength of 0.1, 1 and 10; $\nu=0.3$.

3. Characterization of axisymmetric SAW motor

3.1. General

As shown in Fig. 1b, two SAW generating units are mounted on a rod. Each unit is for one direction of motion. The SAW will travel in axial direction on the rod. The slider has the fundamental geometry of a hollow cylinder, which generates the contact pressure by a transition or interference fit. Using piezoelectric single crystals for the SAW generating units is problematic. Due to the axial symmetry of the rod, it is impossible to orientate the polarization radial. Furthermore, it is complicated to fit a brittle crystal on the rod. Therefore, we decided to use piezoelectric ceramics for generating SAW, to enable a radial polarization.

3.2. Rod radius to wavelength ratio

Eq. (23) clarifies that the ratio of rod radius to wavelength is an important characteristic. It influences the axial particle velocity on the rod’s surface. This velocity is a measure of the idling speed of the motor.

The particle velocity in radial direction v_r and in axial direction v_z are the derivations of Eq. (23):

$$v_r = aq_A\omega \left(\frac{2k_A^2}{k_A^2 + s_A^2} \frac{I_1(q_A R_o)}{I_1(s_A R_o)} I_1(s_A r) - I_1(q_A r) \right) \cdot \sin(k_{Az} - \omega t),$$

$$v_z = ak_A\omega \left(\frac{2q_A s_A}{k_A^2 + s_A^2} \frac{I_1(q_A R_o)}{I_1(s_A R_o)} I_0(s_A r) - I_0(q_A r) \right) \cdot \cos(k_{Az} - \omega t). \tag{28}$$

Thus, with $r = R_o$ the maximum particle velocity on the rod’s surface in radial direction, \hat{v}_{rS} and in axial direction \hat{v}_{zS} are:

$$\hat{v}_{rS} = aq_A\omega \left(\frac{2k_A^2}{k_A^2 + s_A^2} \frac{I_1(q_A R_o)}{I_1(s_A R_o)} I_1(s_A R_o) - I_1(q_A R_o) \right),$$

$$\hat{v}_{zS} = ak_A\omega \left(\frac{2q_A s_A}{k_A^2 + s_A^2} \frac{I_1(q_A R_o)}{I_1(s_A R_o)} I_0(s_A R_o) - I_0(q_A R_o) \right). \tag{29}$$

The numerically calculated maximum axial particle velocity on the surface, normalized to the negative maximum radial particle velocity

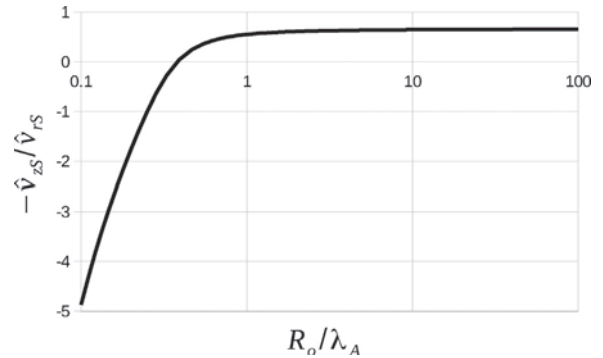


Fig. 5. Theoretical axial surface velocity normalized to radial surface velocity as a function of rod radius normalized to wavelength; $\nu=0.3$.

ity on the surface, is shown in Fig. 5. It is obvious that the relative axial velocity is nearly constant for a rod radius to wavelength ratio larger than 1. For a ratio lower than about 0.4 the traveling direction is changing. Thus, a slider movement in traveling wave direction would be possible in theory. However, due to the low frequency, the absolute velocity is very low. Moreover, normalized to the wave power the square of axial velocity decreases commonly with the rod radius. This effect is presented in Fig. 6. We chose the square of axial velocity because kinetic energy is defined as $E_{kin} = mv^2/2$ with the mass m and the general velocity v . For the SAW on a rod the infinitesimal kinetic energy is:

$$\frac{\partial^3 E_{kinA}}{r \partial z \partial r \partial \theta} = \frac{\rho_0(v_z^2 + v_r^2)}{2}. \tag{30}$$

θ is the angular coordinate of the cylindrical coordinate system. In general the potential energy is defined as $E_{pot} = V\sigma\epsilon/2$ with the volume V . So we can define the infinitesimal potential energy in similar fashion:

$$\frac{\partial^3 E_{potA}}{r \partial z \partial r \partial \theta} = \frac{\vec{\sigma} \cdot \vec{\epsilon}}{2}. \tag{31}$$

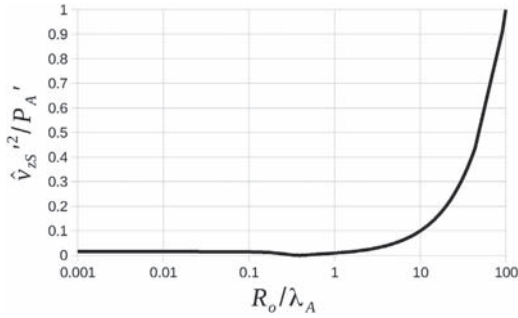


Fig. 6. Normalized ratio of squared theoretical axial surface velocity to wave power as a function of rod radius normalized to wavelength; normalized theoretical axial surface velocity is $\hat{v}_{zS} = \hat{v}_{zS}(R_0/\lambda_A)/\hat{v}_{zS}(R_0/\lambda_A = 100)$; Normalized wave power is $P_A = P_A(R_0/\lambda_A)/P_A(R_0/\lambda_A = 100)$; $\nu = 0.3$.

Thus, for the length of one wavelength, the overall energy $E_{A|0}^{\Lambda A}$ is the sum of kinetic and potential energy $E_{kinA|0}^{\Lambda A}$ and $E_{potA|0}^{\Lambda A}$, respectively:

$$E_{A|0}^{\Lambda A} = \int_0^{R_0} \int_0^{\Lambda_A} \pi r (\rho_0(v_z^2 + v_r^2) + \vec{\sigma} \cdot \vec{\epsilon}) dz dr. \quad (32)$$

Thus, we can define the wave power as:

$$P_A = E_{A|0}^{\Lambda A} f. \quad (33)$$

The increase of axial surface velocity, depending on increasing rod radius, results from the decreasing relative thickness of the outer region with relevant motion, as shown in Fig. 4. Thus, nearly the whole energy of the SAW is near the surface. This results in the following findings: The rod radius to wavelength ratio should not be smaller than 1. So for high force design it should approach 1. For high speed design the ratio should be as big as possible. Thus, it is possible to characterize the motor for a specific area of application. With respect to a miniaturization, the minimum wavelength at a given rod radius is limited by material properties and technological boundaries. On the one hand, the SAW generating unit must also become miniaturized. On the other hand, a higher frequency means both higher material damping and a lower penetration depth and a lower particle deflection on the rod’s surface. Therefore a higher surface finish of stator and slider is needed to avoid high damping and interlocking of stator and slider surface, respectively.

3.3. Efficiency, idling speed and blocking force for simplified model

In general, work is defined as the product of force and displacement. Thus, the infinitesimal loss of wave energy under the slider can be defined as:

$$\frac{\partial E_A(z)}{\partial z} = MF_N C_5 \hat{u}_{zS}(E_A(z)). \quad (34)$$

F_N is the normal force, M is the friction coefficient and C_5 determines the proportion of the axial particle displacement amplitude at the rod’s surface \hat{u}_{zS} that is responsible for the energy drain. Eq. (32) demonstrates that the wave energy depends on the square of the amplitude a . In consideration of Eq. (23), we can say that \hat{u}_{zS} is proportional to the square root of the infinitesimal loss of wave energy:

$$\frac{\partial E_A(z)}{\partial z} = C_6 \sqrt{E_A(z)}. \quad (35)$$

C_6 is a temporarily used constant. The solution of this differential equation is:

$$E_A(z) = \left(\frac{C_6}{2} (z + C_7) \right)^2. \quad (36)$$

C_7 is the integration constant. Similar to the axial particle displacement amplitude at the rod’s surface \hat{u}_{zS} , we find a squared dependence between wave energy and particle velocity via Eqs. (32) and (29). Thus, based on Eq. (36) we can find a linear decrease of the axial particle velocity amplitude on the rod’s surface under the slider:

$$\hat{v}_{zS}(z) = v_0 + (v_l - v_0) \frac{z}{l}. \quad (37)$$

l is the slider length according to Fig. 7a. v_0 and v_l are the axial particle velocity amplitudes on the rod’s surface in front of and behind the slider, respectively. To simplify, we assume that the slider has only contact with the peaks of the SAW. If the slider speed v_{sl} is v_0 or higher, the whole slider would be pushed in traveling wave direction by the friction force. If the slider had a speed of v_l or lower, the whole slider would be pushed in the opposite direction. For a speed between v_0 and v_l the output force is

$$F_{out} = -F_f + F_b = MF_N \frac{z(v_{sl})}{l} - MF_N \frac{l - z(v_{sl})}{l} = MF_N \left(\frac{2z(v_{sl})}{l} - 1 \right). \quad (38)$$

F_f is the force acting forward, F_b the force acting backwards and $z(v_{sl})$ the position under the slider, where the axial particle velocity on the rod’s surface equals the slider speed. With Eq. (37) we can describe it as follows:

$$z(v_{sl}) = l \frac{v_{sl} - v_0}{v_l - v_0}, \quad (0 < v_l < v_0, v_l \leq v_{sl} \leq v_0). \quad (39)$$

For a constant normal force, the output power can be defined as

$$P_{out}(v_{sl}) = F_{out}(v_{sl}) v_{sl}. \quad (40)$$

Substituting Eqs. (38) and (39) into Eq. (40) yields

$$P_{out}(v_{sl}) = MF_N \left(2 \frac{v_{sl} - v_0}{v_l - v_0} - 1 \right) v_{sl}, \quad (0 < v_l < v_0, v_l \leq v_{sl} \leq v_0). \quad (41)$$

This output power has no local extreme within its domain. Thus, the maximum output power is defined for $v_{sl} = v_l$:

$$P_{outmax} = P_{out}(v_l) = MF_N v_l. \quad (42)$$

Considering a simplified linear relation between output force and slider speed $v_{sl} = v_l$ according to Fig. 7b, the maximum output power occurs for $v_{sl} = v_l = v_0/2$. Considering Eqs. (29), (32) and (33) we can say that the SAW power is proportional to the square of \hat{v}_{zS} . So we can calculate the maximum efficiency as follows:

$$\eta_{max} = \frac{P_A(0) - P_A(l)}{P_A(0)} = \frac{v_0^2 - (v_0/2)^2}{v_0^2} = 0.75. \quad (43)$$

According to Eq. (38) the output force is zero for $z = l/2$. Therefore, we can derive the idling speed from Eq. (37) as follows:

$$v_{idl} = v_0 + \left(\frac{v_0}{2} - v_0 \right) \frac{l}{2l} = 0.75 v_0. \quad (44)$$

As the relation between the axial particle velocity on the rod’s surface and wave power is known from Eq. (33), we can describe the blocking force using Eqs. (40) and (43) as follows:

$$F_{bl} = MF_N = \frac{P_{out}}{v_{sl}} = \frac{2 \cdot 0.75 P_A(0)}{v_0} = 1.5 \frac{P_A(0)}{v_0}. \quad (45)$$

Of course this is just a simple theoretical model showing the general motor behavior. It ignores several losses like SAW excitation losses. Furthermore, caused by the slider’s elasticity it contacts the stator not only at the wave peaks. Thus, the slider can be accelerated and decelerated by the same wave crest, which results in power losses. Therefore [14] states an overall efficiency of 2% for a plane SAW motor using a LiNbO₃ stator. However, it is possible to recover a part of the remaining wave power to improve the efficiency. This method is also described in [14].

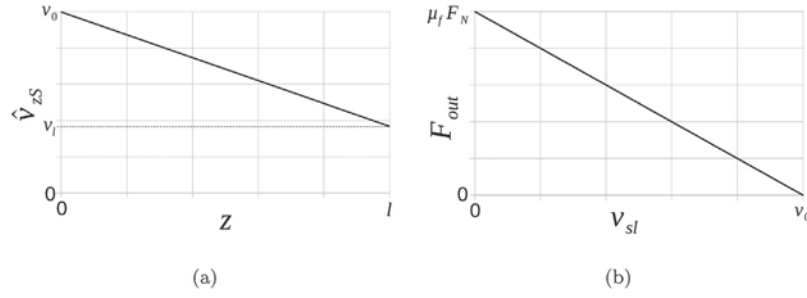


Fig. 7. (a) Assumed linear axial particle velocity decrease on the rod's surface under the slider; (b) assumed slider speed to output force ratio for $v_{sl} = v_l$.

3.4. Exemplary motor parameters

Based on the presented derivations, some basic parameters for an exemplary motor can be calculated.

According to Eq. (25), the wave velocity c_A would be about 3000 m s^{-1} for a steel rod with a diameter of 4 mm, depending on the actual wavelength. With reference to Section 3.2, we can choose a specific ratio of $R_0/\Lambda_A = 1$ for high force design. In this case, according to Eqs. (25) and (27), the wave frequency is 1.52 MHz. By linking Eq. (33) to Eqs. (29) and (23) via the amplitude a we can calculate an axial velocity amplitude of 114 mm s^{-1} and a radial displacement amplitude of 21 nm, respectively, for particle on the rod's surface and a wave power of 5 W. Corresponding to Eqs. (44) and (45), we calculated an idling speed of 85 mm s^{-1} and a blocking force of 66 N, respectively, for the simplified model, presented in Section 3.3.

The rod radius to wavelength ratio for high speed design is just limited by material properties and technological boundaries. As an example we present motor parameters for a ratio of 10 in a similar fashion. The appropriate wave frequency is 14.9 MHz. For the same wave power of 5 W the axial surface velocity rises to 378 mm s^{-1} , the radial amplitude drops to 6.1 nm at the surface. In accordance with the simplified model, results show a higher idling speed of 283 mm s^{-1} and a blocking force of only 20 N.

4. SAW motor with a plane stator made from non-piezoelectric material

The SAW motor we present within this Section is a plane one, since it is one step towards the mentioned axisymmetric SAW motor. Nevertheless, it is the first SAW motor with a stator made from non-piezoelectric material and consequently fundamentally different from the motors presented in [8], [15], etc.

4.1. Realization

We built up a slider, which fits to the one presented by [10]. It has a size of $6 \text{ mm} \times 6 \text{ mm} \times 525 \text{ }\mu\text{m}$. At the bottom of the slider there are 16,560 projections with a diameter of $22.5 \text{ }\mu\text{m}$ and a height of $2 \text{ }\mu\text{m}$. They are arranged in a rectangular area with a size of $4 \text{ mm} \times 4 \text{ mm}$ and provide the contact to the stator. Our solution differs from the slider presented in [10] by a hexagonal rather than a rectangular projection arrangement, as shown in Fig. 8. Consequently it results in a higher projection amount on the same area.

On the one hand, the slider requires a small contact surface and a resulting higher contact pressure in order to avoid a film of air between stator and slider. Kurosawa [9] introduced the structured slider for this reason. On the other hand, the working principle of an SAW motor is based on the alternation between contact and no contact of the slider. If the contact surface is too small, the elasticity in normal direction to the surface will be so high that there is a permanent contact. So there is an optimum for the amount of projections on a slider. Shigematsu and Kurosawa present a quasistatic

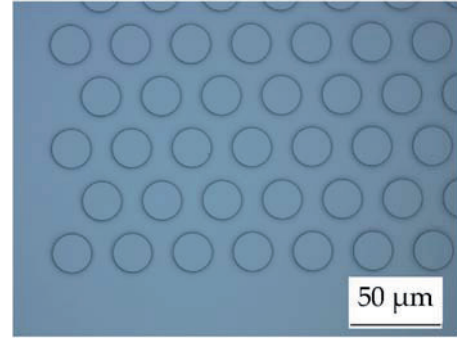


Fig. 8. Projections on the slider contact surface in hexagonal arrangement.

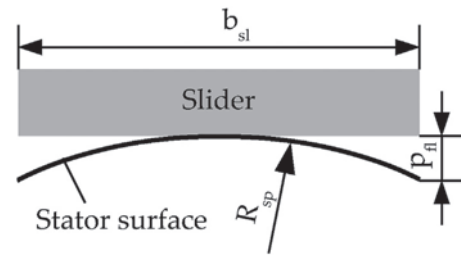


Fig. 9. Spherical flatness p_{fl} of stator surface with the resulting gap between stator and slider.

numeric model, which considers the elasticity of stator and slider for every projection [16–18]. They use it to find the optimum number of projections and the appropriate projection diameter. Based on their experimental results, they introduced an effective factor with an amount of 0.6. It determines the relative amount of projections in one line that have contact with the stator within one period time. As this factor depends on production tolerances, we use this numerical model and determine the effective factor by flatness and roughness of the stator. In our case we assume much higher tolerances of the stator towards the slider, as the slider is produced by semiconductor technology.

Assuming a spherical shape of the stator, we are able to determine a relation between flatness and effective factor by Hertzian contact. According to Fig. 9, the sphere radius R_{sp} results from the flatness p_{fl} and the width b_{sl} of the slider as follows:

$$R_{sp} = \frac{p_{fl}}{2} + \frac{b_{sl}^2}{8p_{fl}}. \quad (46)$$

Then we can describe the contact radius R_c with [19]:

$$R_c = \sqrt[3]{\frac{3F_N R_{sp}}{4D^*}}, \quad (47)$$

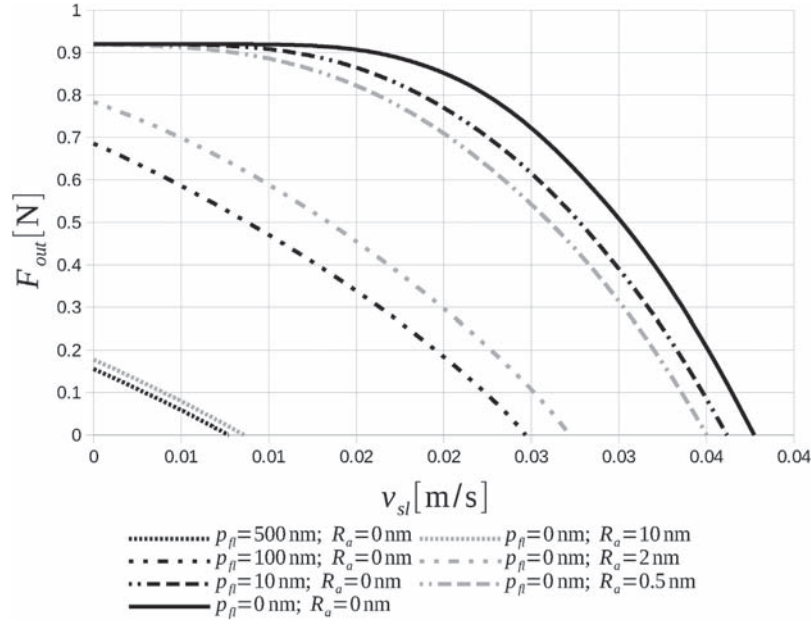


Fig. 10. Slider speed to output force ratios calculated with numeric model for several flatness and roughness specifications; stator material: steel; slider material: silicon; $f=3.7$ MHz; maximum normal SAW amplitude $\hat{u}_{zS} = 3$ nm; $M=0.23$; $b_{sl}=4$ mm; number of projections: 100×100 ; projection diameter: $20 \mu\text{m}$; projection height: $2 \mu\text{m}$; $F_N=4$ N.

$$\text{with } \frac{1}{D^*} = \frac{1 - \nu_{st}^2}{D_{st}} + \frac{1 - \nu_{sl}^2}{D_{sl}}.$$

D_{sl} and D_{st} are the Young’s moduli of the slider and the stator, respectively, and ν_{sl} and ν_{st} are the Poisson’s ratios of the slider and the stator, respectively. After that we can calculate the relative contact area A' by dividing the contact area A_c by the slider base A_{sl} :

$$A' = \frac{A_c}{A_{sl}} = \frac{\pi R_c^2}{b_{sl}^2}. \quad (48)$$

As the effective factor is defined as the contact relation within a projection line, this factor can be calculated as follows:

$$\eta_{fl} = \sqrt{A'} = \frac{\sqrt{\pi}}{b_{sl}} R_c = \frac{\sqrt{\pi}}{b_{sl}} \sqrt[3]{\frac{3F_N R_{sp}}{4D^*}}. \quad (49)$$

Supposing a very large number of projections and a Gaussian distribution of the stator’s surface height, we can determine an effective factor by roughness. Assuming a fixed stator, we must find the normal displacement of the slider u_{sln} for a given normal force F_N . Starting far away from the stator, we can shift the slider towards the stator. First we have very few projections which will be compressed due to the Gaussian distribution. But the more the slider approaches to the stator, the more projections will be compressed, until nearly all projections will be compressed. We must shift the slider towards the stator until the compression force fits to the given normal force. The associated equation is:

$$F_N = n_{pr} K_{ovn} \int_{-\infty}^{u_{sln}} N(u_n, R_a) du_n. \quad (50)$$

n_{pr} is the number of all slider’s projections and K_{ovn} is the overall stiffness in normal direction of stator and slider, considering one projection. $N(u_n, R_a)$ is the cumulative distribution function of the stator’s surface height as a function of the position in normal direction u_n and its standard deviation R_a , which equals to the average surface finish. The mean of the distribution is attained as zero. This

equation can be solved numerically. Using the computed u_{sln} , we can determine the effective factor for roughness by:

$$\eta_{ro} = \sqrt{N(u_{sln}, R_a)}. \quad (51)$$

Fig. 10 shows several motor characteristics calculated with Shigematsu’s and Kurosawa’s numeric model, expanded by the mentioned flatness and roughness dependence. We can see that the flatness should be lower than 500 nm and the roughness lower than 10 nm.

We realized the stator by bonding a PZT plate with a thickness of 0.2 mm on a steel substrate by epoxy resin. The PZT plate has a sputtered base electrode used for polarization. An inter-digital transducer (IDT) is placed on the PZT plate with a finger spacing of half SAW wavelength. It is made by thick film technology. The actuator is designed for using the piezoelectric plate as alternating thickness oscillators when an alternating voltage is applied on the top electrodes. Therefore, a symmetric mode will be stimulated. This oscillation in turn stimulates the SAW. The natural frequency of the PZT plate is given by its thickness. For SAW generation the natural frequency must fit with the SAW frequency, which is defined by the SAW sound velocity and the SAW wavelength. To determine this wavelength we built up a 2D finite element model (FEM), which uses two symmetry planes normal to the direction of SAW propagation bisecting the finger-shaped top electrodes as shown in Fig. 11. Simplified there is no displacement in the direction of propagation at its boundaries. The mesh size is $\Lambda_p/25 \times \Lambda_p/25$, whereas Λ_p is the wavelength of the Rayleigh wave on plane surface. We made modal analyses to find the SAW frequency close to the natural frequency. As this model fits only for an infinite actuator, we built up another 2D model with the whole adhered actuator and extended the substrate on both sides. The outer regions are implemented with high material damping to avoid reflections. The mesh size is $\Lambda_p/25 \times \Lambda_p/25$ near the stimulated surface. Within the steel plate, the element height normal to the stimulated surface rises continuously to $\Lambda_p/2.5$ at the opposite surface. We considered the piezoelectric behavior and made a transient simulation with a time step size of $1/40f$. A sinusoidal voltage was applied to the IDT. With this model we corrected the previously determined SAW frequency.

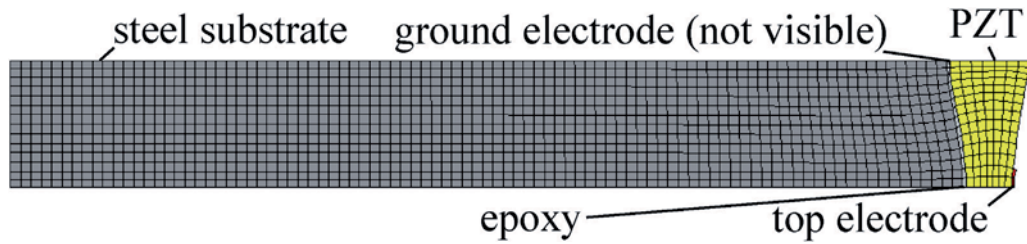


Fig. 11. FEM model of plane stator section: deformed mesh resulting from modal analysis with symmetric mode oscillation of PZT layer.

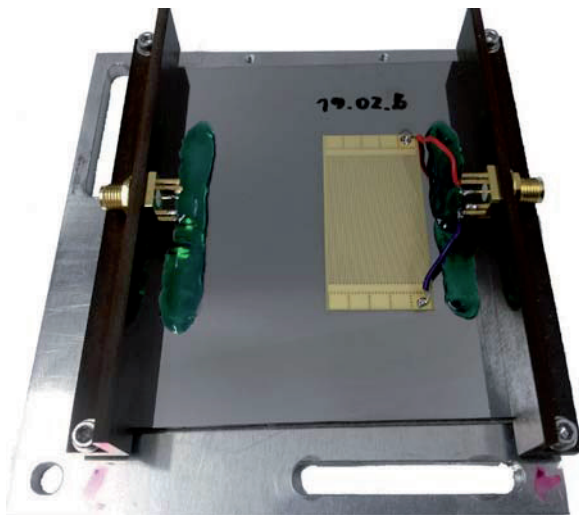


Fig. 12. Stator made from steel with SAW generating unit mounted on holder.

Fig. 12 shows a manufactured stator made with a steel substrate. The PZT plate is made from the material Sonox P53 produced by CeramTec GmbH. Latex films have been applied for damping in the directions of SAW's travel. The substrate thickness is 3 mm. The thicknesses of epoxy layer, ground electrode, PZT layer and top electrode are 10 μm , 0.3 μm , 200 μm and 8 μm , respectively. The wavelength, determined by finger electrode distance, is 800 μm . The IDT has 30 finger pairs with an overlapping finger length of 35.9 mm. The stator surface is lapped and polished with a flatness of 8 μm . Ground electrode and IDTs are made from gold.

After manufacturing the prototype we manually applied a conductive silver lacquer on the piezoelectric layer for the polarization. Then an electrostatic field of 2 MV m^{-1} was applied between the bottom electrode and the silver layer. After that we removed the silver layer.

4.2. Results

This section presents a manufactured plane SAW motor, as mentioned in Section 4.1. Its electric behavior and optical measured SAW are discussed and compared to a FEM model. Based on these measurements, we calculate the efficiency of the manufactured stator. Furthermore, we present characteristic motor parameters.

For comparison of stator behavior we use the 2D FEM simulation, mentioned in Section 4.1. By implementing transient simulations for a set of frequencies, we can determine displacements of the SAW and the impedance of the SAW generating unit by reading the time dependent electric charge of the electrodes. As the FEM model does not consider the dielectric loss, we determine the frequency dependent impedance of an unpolarized SAW generating unit with a network analyzer. The resulting dielectric

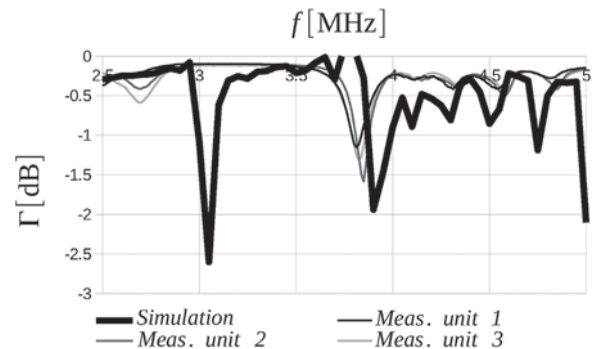


Fig. 13. Reflection coefficient of one simulated and three different measured SAW generating units as a function of frequency from 2.5 to 5 MHz; each measured graph represents the average of ten measurements.

loss of about $\tan \delta = 0.4$ at a frequency of 3.85 MHz is considered as a series impedance behind the simulated impedances, discussed subsequently.

The frequency dependent reflection coefficient of a polarized SAW generating unit, measured with a network analyzer, is shown in Fig. 13 for 50 Ω internal resistance. The simulated reflection coefficient is displayed too. At 3.85 MHz the symmetric mode oscillation of the PZT can be obtained. Fig. 13 reveals that the frequencies are slightly shifted between measurement and simulation. This is caused by the slightly different material parameters. It is obvious that at resonance frequencies with a reflection coefficient of about -1.3 dB the transmission is well perceptible. However, it is less significant than in the simulation due to a lower piezoelectric coupling coefficient compared to simulation. For comparison Fig. 14 presents the real and the imaginary parts of the measured and simulated impedances as well as the real part of the simulated impedance, neglecting the dielectric loss too. The high reflection coefficient for resonance frequencies results from the bad adjustment at 50 Ω . The low reflection at 3.05 MHz in simulation is noticeable. It is caused by the antisymmetric mode oscillation of the PZT according to Fig. 15. The associated measured resonances can be found at lower frequency with a lower intensity.

We performed vibrometer measurements with a Polytec UHF-120 of the manufactured SAW generating unit, denoted as *Meas. unit 2* in Fig. 13. The measured displacements represent an average over ten single measurements for 30 separate measurement points close to the SAW generating unit. This revealed orthogonal steel substrate displacements of 314 pm at $U_{op} = 1 \text{ V}$ for the symmetric mode oscillation of the PZT layer. The 2D simulation model provides displacements which are averaged over 10 periods and three separate points on the substrate's surface. We took dielectric loss of $\tan \delta = 0.4$ into account for the presented displacements. Thereby the simulated displacement for symmetric mode oscillation is significantly higher than the measured displacement with 4260 pm at 3.65 MHz. This mismatch between simulation and

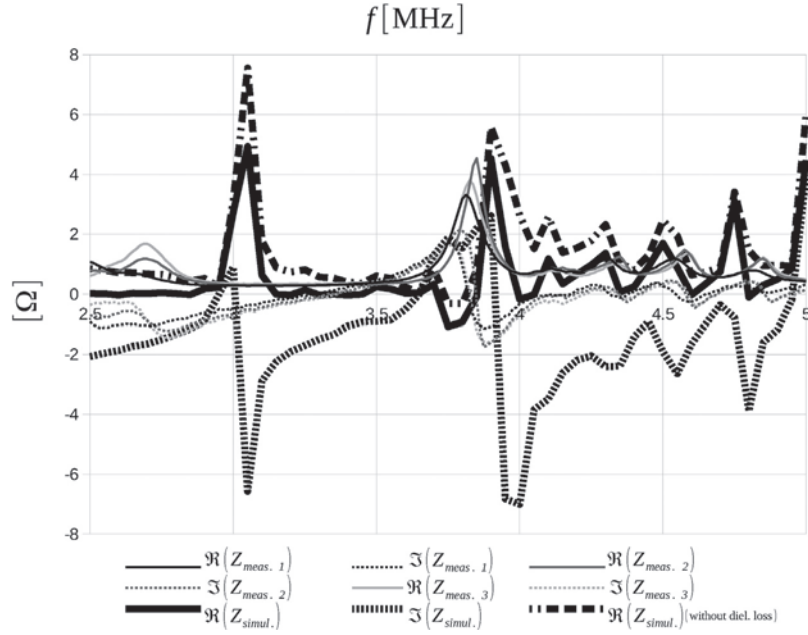


Fig. 14. Impedances of one simulated and three different measured SAW generating units as a function of frequency; each measured graph represents the average of ten measurements; for comparison the real part of the simulated impedance is presented, neglecting dielectric loss.

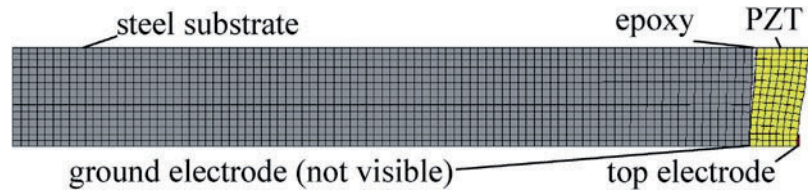


Fig. 15. FEM model of plane stator section: deformed mesh resulting from modal analysis with antisymmetric mode oscillation of PZT layer.

measurement results from the much lower impedance of the simulated SAW generating unit at resonance frequency according to Fig. 14.

We performed a further measurement at a distance of 26.5 mm towards the first measurement. Due to the decline of displacement amplitude to 237 pm, we can calculate a spatial amplitude attenuation coefficient of $\alpha = 0.09 \text{ dB mm}^{-1}$ for the steel substrate. We assume it is mainly caused by scattering of Rayleigh wave normal to the traveling direction and by a grain size in a similar order of the wavelength. This decrease is not negligible, but suitable for traveling distances in the order of 10 mm.

For calculating the efficiency of the manufactured prototypes, we can use the equations for determining the tangential and normal displacement of Rayleigh waves at a plane surface u_x and u_z , respectively, described by [12]:

$$\begin{aligned} u_x &= ak_p \left(e^{-q_p z} - \frac{2q_p s_p}{k_p^2 + s_p^2} e^{-s_p z} \right) \sin(k_p x - \omega t), \\ u_z &= aq_p \left(e^{-q_p z} - \frac{2k_p^2}{k_p^2 + s_p^2} e^{-s_p z} \right) \cos(k_p x - \omega t). \end{aligned} \quad (52)$$

$k_p \approx (0.87 + 1.12\nu)/1 + \nu$, $q_p^2 = k_p^2 - k_L^2$ and $s_p^2 = k_p^2 - k_T^2$ are parameters for the plane Rayleigh wave. x and z are the abscissa and apply of the Cartesian coordinate system, respectively. This Rayleigh wave is traveling in the x -direction and the surface is at $z = 0$, whereas the positive z -direction points into the solid.

Based on Eq. (52), we can determine the power of the plane wave similar to Eq. (33):

$$\begin{aligned} P_P &= f(E_{kinP}|_0^{\Lambda_P} + E_{potP}|_0^{\Lambda_P}) = \frac{fb_{IDT}}{2} \int_0^\infty \int_0^{\Lambda_P} \rho_0 (v_x^2 + v_z^2) \\ &+ \vec{\sigma}_c \cdot \vec{\epsilon}_c \, dx \, dz = \frac{a^2 fb_{IDT}}{2} \int_0^\infty \int_0^{\Lambda_P} \rho_0 \left(\left(\frac{\partial u_x}{\partial t} \right)^2 + \left(\frac{\partial u_z}{\partial t} \right)^2 \right) \\ &+ \frac{\vec{\sigma}_c(u_x, u_z) \cdot \vec{\epsilon}_c(u_x, u_z)}{a^2} \, dx \, dz. \end{aligned} \quad (53)$$

$E_{kinP}|_0^{\Lambda_P}$ and $E_{potP}|_0^{\Lambda_P}$ are the kinetic and potential energy of the plane Rayleigh wave, respectively, for the length of one wavelength Λ_P . b_{IDT} is the width of the IDT, v_x and v_z are the particle velocities in x - and z -direction, respectively, and $\vec{\sigma}_c$ and $\vec{\epsilon}_c$ are the stress and strain tensors in Cartesian coordinates, respectively. a can be determined by Eq. (52) for $z = 0$ and the measured displacement as u_z . Thus, we get the power of the measured Rayleigh wave with 9.9 mW at an applied voltage of $U_{0p} = 1 \text{ V}$ for the symmetric mode oscillation. The following equation describes the power consumption of the whole SAW generating unit:

$$P_{el} = 0.5 \Re \left(\frac{U_{0p}^2}{Z} \right). \quad (54)$$

Z is the impedance of the SAW generating unit according to Fig. 14. The factor 0.5 considers the fact that SAW leave the SAW generating unit in two directions. For the symmetric mode oscillation we get a power consumption of 58.6 mW, which yields an efficiency of 17% for SAW generation. When comparing with IDT structures on LiNbO₃ single crystals, the efficiency is low due to negligible internal losses in the substrate material. For example [20] presents a

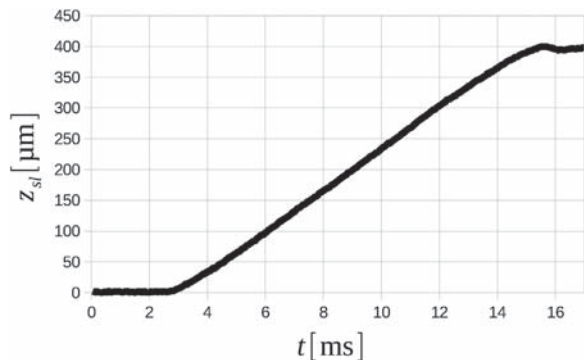


Fig. 16. Slider position z_{sl} as a function of time; applied voltage amplitude: 50 V; number of periods: 50,000.

delay line with two IDT structures and a loss of 2.5 dB. This leads to a minimum efficiency of 75% for SAW generation with one IDT structure on LiNbO₃ single crystal.

For motor characterization, we ran the stator at 3.85 MHz with a voltage amplitude of 50 V over 50,000 periods. The slider was pressed onto the stator with a permanent magnet, yielding a force of 1.14 N. Our measurement equipment was a laser triangulation sensor Keyence LK-G82 and a force gauge Imada DPX for position and force measurement, respectively. An exemplary time dependent slider shift is presented in Fig. 16. We measured an idling speed of 29 mm s⁻¹ and the motor achieved blocking forces of 0.19 N. Idling speed and blocking force are averaged over 10 single measurements. These motor parameter are considerably smaller than the idling speed of 0.7 m s⁻¹ and the blocking force of 10 N, mentioned for the known SAW motor in [10]. We assume that major reasons are the lower losses of LiNbO₃ and the flatter surface of such single crystal stator. This results in a higher amount of projections that have contact with the stator as mentioned in Section 4.1. Nevertheless, the presented motor is the first working model of a SAW motor with a non-piezoelectric stator.

5. Generation of SAW on non-piezoelectric material by thick film actuator

As mentioned in Section 3.1, we decided in favor of SAW generating units made from piezoelectric ceramics which must be fitted on the stator. However, the deflections of the piezoelectric material are in the nanometer or even picometer range. Furthermore, typical piezoelectric ceramics have a low fracture strain and high manufacturing tolerances. Therefore, an interference fit is not appropriate to transfer these displacements on the stator if we want to build up an axisymmetric SAW motor. A valid option is to fit the piezoelectric ceramic by soldering or adherence. A third option is to fire the ceramic directly on the stator base material. Assuming soldering or gluing we need a piezoelectric ceramic with the shape of a tube or flexible actuators as mentioned in [21]. Such a flexible device with a lower ceramic content must be wrapped around the stator rod. Soldering a tube is very ambitious, since the solder must flow through a long narrow gap. Gluing a tube or flexible piezoelectric material has the disadvantage of a relative low Young's modulus of the glue. Thus, depending on the gap height, at operation the transition would offer a high acoustic reflection coefficient. Firing ceramics directly on the stator base material can be ambitious, as stator base material must withstand temperatures of about 800 °C. However, ceramics which are fired directly on stator base material are solid and directly connected to the stator. Beside this, we have the option of manufacturing piezoelectric ceramics by thick film technology. This technology allows the realization of these units on cylindrical rods. Therefore, round printing can be used as shown

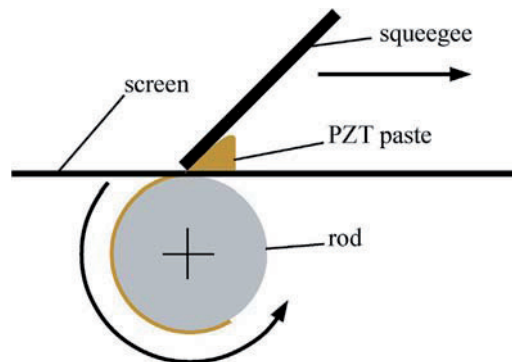


Fig. 17. Schematic sketch of round printing with screen: the rod is rolled under the stationary screen as fast as the squeegee.

in Fig. 17. Consequently, within this Section we present a plane stator made by thick film technology. It cannot be used to move a slider due to too high flatness values of the stator's surface. Nevertheless, generating SAW by thick film actuator is a crucial step towards the mentioned axisymmetric SAW motor.

5.1. Realization

As various materials as stator base material have been tested, we discuss possible substrate materials for the mentioned printing process within this paragraph, namely some ceramics, titanate and steel. Sintered substrate materials like Al₂O₃, ZrO₂ and LTCC are established for printing lead zirconate titanate (PZT) layers by thick film technology [22]. However, sintered materials are not homogeneous and will strongly dampen the SAW. For instance [23] states an attenuation of 42% for a half inch sample of Al₂O₃ with a porosity of 7% at a frequency of 10 MHz. Owing to this and its brittle behavior, sintered materials are not well suited materials. Metals with a homogeneous structure and a tough behavior would be preferable. Titanium is a metal with a suitable coefficient of thermal expansion. However the layers need to be fired at about 800 °C. At this temperature its oxidation is too high. Thus, a sufficient adhesion is not possible between titanium and the printed layers. A common material is steel. Its physical properties can be modified by varying alloy. However, steel as substrate material has disadvantages too. Depending on the specific type of steel, oxidation is too high at this temperature. Furthermore, the printed layers could be sheared off during cooling down due to the relatively high coefficient of thermal expansion. However steel 1.4016 is a ferritic stainless steel with moderate oxidation. Due to ferritic behavior this steel has a relatively low thermal expansion. Thus, it is possible to use that steel as a substrate for the thick film variant. For the subsequent work we focus on substrates of steel 1.4016.

The structure of the SAW generating unit differs from the one presented in Section 4 as follows. We add an isolation layer between substrate and ground electrode to ensure an adhesion. Therefore, we do not apply an epoxy resin film as described in Section 4. All four layers are printed by thick film technology. We used FEM models, as described in Section 4, to determine the PZT thickness. Fig. 18 shows a manufactured stator made with a steel substrate. Latex films have been applied behind the IDTs for damping. The substrate thickness is 3 mm. The thicknesses of isolation layer, ground electrode, PZT layer and top electrode are 25 µm, 12 µm, 151 µm and 8 µm, respectively. The wavelength, determined by finger electrode distance, is 560 µm. Each IDT has 8 finger pairs with an overlapping finger length of 26.4 mm and between the SAW generating units there is a gap of 33 mm. That region is polished, enabling a better measurement quality. Ground electrode and IDTs are made from gold.

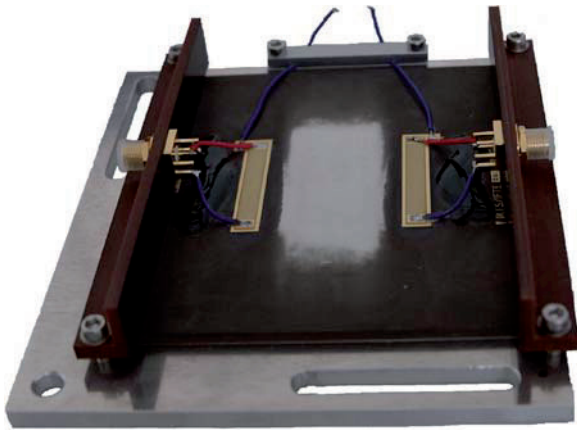


Fig. 18. Steel substrate with two SAW generating units used for optical and impedance measurements and mounted on holder; the two long blue wires are connected with ground electrode and have been used for polarization; the area in the center of the substrate is polished to enable optical measurement.

These prototypes have been polarized in the same way as the adhered stators.

5.2. Results

This section presents electric and acoustic behavior of the manufactured plane stators, mentioned in Section 5.1. The results are discussed and compared to a FEM model, similar to Section 4.2. Based on these measurements, we calculate the efficiency of the manufactured stator. The steel surface will be oxidated after firing the SAW generating unit. For this reason, flatness and roughness cannot be enabled by lapping and polishing before firing the SAW generating unit. At this point, motor parameters for this thick film actuator cannot be presented as it is not easy to lap the stator surface close to the adjacent previously applied SAW generating unit.

For comparison we use the 2D FEM simulation, again. We used the material PZT-8 for the piezoelectric material. However, the piezoelectric coupling coefficients $d_{31} = -60 \times 10^{-12} \text{ mV}^{-1}$, $d_{33} = 140 \times 10^{-12} \text{ mV}^{-1}$ and $d_{15} = 205 \times 10^{-12} \text{ mV}^{-1}$ were adapted from PZT-8 by a linear scaling to $d_{33} = 140 \times 10^{-12} \text{ mV}^{-1}$, which is given for the PZT we used. It was determined by a capacitive detector for the PZT, printed on LTCC [22]. The experimentally determined dielectric loss of about $\tan \delta = 0.195$ at a frequency of 5 MHz is considered as a series impedance behind the simulated impedances.

The frequency dependent reflection coefficient of a polarized SAW generating unit, measured with a network analyzer, is shown in Fig. 19 for 50Ω internal resistance. The simulated reflection coefficient is displayed too. At 5.5 MHz the symmetric mode oscillation of the PZT can be obtained. At 4.15 MHz a Rayleigh wave is generated as well. This oscillation can be seen in simulation too. It is stimulated by an antisymmetric oscillation mode similar to the adhered stator, presented in Section 4. Due to the lower frequency of that mode, the SAW accelerates when leaving the piezoelectric layer, and its wavelength is increasing. Fig. 19 reveals that the frequencies are slightly shifted between measurement and simulation owing to the slightly different material parameters of PZT-8 used for simulation. It is obvious that at resonance frequencies with a reflection coefficient of about -1.5 dB the transmission is well perceptible. However, it is less significant than in the simulation due to a lower piezoelectric coupling coefficient compared to simulation. Furthermore, aside from the resonances, the measured loss is about 1.2 dB , mainly due to the dielectric loss. For comparison Fig. 20 presents the real and the imaginary parts of the measured

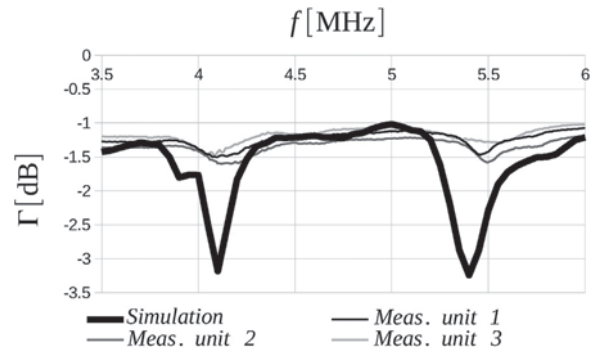


Fig. 19. Reflection coefficient of one simulated and three different measured SAW generating units as a function of frequency; each measured graph represents the average of ten measurements.

and simulated impedances as well as the real part of the simulated impedance, neglecting the dielectric loss too.

The vibrometer measurements of the manufactured SAW generating unit, denoted as *Meas. unit 1* in Fig. 19 are an average over ten single measurements for 30 separate measurement points close to the SAW generating unit, again. This revealed orthogonal steel substrate displacements of 34 pm at $U_{op} = 1 \text{ V}$ for the symmetric mode oscillation of the PZT layer and 49 pm at $U_{op} = 1 \text{ V}$ for the antisymmetric mode. The 2D simulation model provides displacements which are averaged over 10 periods and three separate points on the substrate's surface. We took dielectric loss of $\tan \delta = 0.195$ into account for the presented displacements. Thereby the simulated displacement for symmetric mode oscillation is much higher than the measured displacement with 182 pm at 5.35 MHz . The simulated displacement caused by antisymmetric oscillation modes of piezoelectric layer is 82 pm at 4.00 MHz , which is two third larger than the measured displacement. So the vibrometer measurements show a better wave transmission caused by antisymmetric modes in opposite to the simulation model. The simulation model renders a clear resonant vibration of the PZT layer at 4.00 MHz visible, but hardly any wave transmission. Within the simulation model, the rectangular junction between PZT layer and exposed ground electrode operates as a reflector. We assume that a smoother junction due to lower manufacturing accuracy enables a better acceleration of SAW, when leaving the PZT layer. Thus we started a further simulation with a smoother junction between PZT and exposed ground electrode. We realized it by an extended PZT layer with an additional length of 6 mm on both sides of the SAW generating unit. Within this junction region we reduced density and stiffness of PZT to zero over twelve equal gradations. This simulation yields displacements of 161 pm at 4.00 MHz and 85 pm at 5.35 MHz . So these simulation results confirm our assumption.

Using Eqs. (53) and (54) we can determine the power of the measured Rayleigh wave with 0.12 mW at an applied voltage of $U_{op} = 1 \text{ V}$ for the symmetric mode oscillation and an appropriate power consumption of 3.70 mW , which yields an efficiency of 3.2% for SAW generation. For the resonance frequency of 4.15 MHz the power of Rayleigh wave is 0.19 mW at $U_{op} = 1 \text{ V}$ and the power consumption of the SAW generating unit is 2.32 mW . This means an efficiency of 8.2% for SAW generation. The efficiency of the thick film actuators is low compared to the presented stator with adhered PZT layer although the dielectric loss is smaller. However, the smaller number of the IDT's finger pairs results in more undesired bulk waves.

6. Conclusion

We extended the theory of Rayleigh waves applied to axisymmetric rods and deduced suitable rod radius to wavelength ratios.

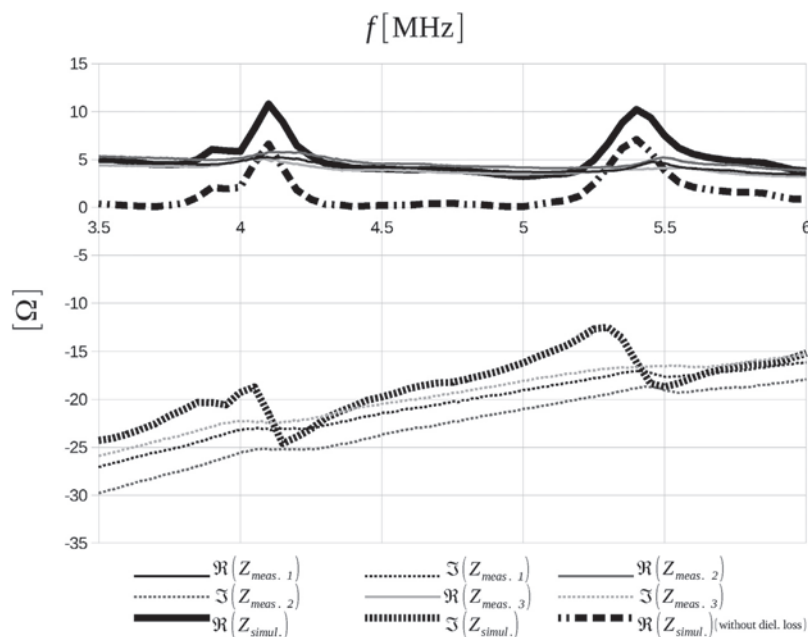


Fig. 20. Impedances of one simulated and three different measured SAW generating units as a function of frequency; each measured graph represents the average of ten measurements; for comparison the real part of the simulated impedance is presented, neglecting dielectric loss.

Based on that derivations we characterized an axisymmetric SAW motor. We were able to show that varying the rod radius to wavelength ratio has a wide influence on dimensioning the blocking force or idling speed. The realizable forces and speeds are in a practice-oriented range.

We presented a plane SAW motor which has an idling speed of 29 mm s^{-1} and a blocking force of 0.19N. It has a very simple design and a tough stator made from non-piezoelectric steel. This promises an inexpensive motor, produced in series, and justifies further investigations.

Furthermore, we presented SAW generating units made by thick film technology on a plane steel substrate to demonstrate that it is basically possible to generate SAW on a non-piezoelectric rod. Appropriate axisymmetric SAW motors could be even simpler in design and would have less efficiency losses for long travel lengths as the Rayleigh waves cannot pass the slider.

The next step is to reduce the high influence of flatness and roughness on plane non-piezoelectric stators to improve slider movement. One possibility is to proceed reducing flatness and roughness values. Another possible approach is to design sliders with adapting surface. After that, the manufacture of an axisymmetric stator by round printing technology and the development of the axisymmetric slider, promising an automatically clamping force, are upcoming tasks too. Efficiencies of 17% for SAW generation allow to proceed the work on SAW motors with non-piezoelectric stator base material. Nevertheless, finding printable piezoelectric material with a lower dielectric loss in the used frequency range is also a promising approach to overcome the currently low efficiency of SAW generation.

Acknowledgments

The authors would like to thank Hagen Schmidt and Robert Weser of the Leibnitz Institute for Solid State and Materials Research Dresden for their friendly expert advice in all technical matters and technical support. Furthermore, we would like to thank Sylvia Gebhardt of the Fraunhofer Institute for Ceramic Technologies and Systems IKTS for her professional advice and technical support relating to the manufacture of thick film PZT actuators.

References

- [1] C. Dinca, *Motor design for maximum material exploitation and magnetization procedure with in-line quality check for mass production*, vol. 1, Universitätsverlag der TU Berlin, 2017.
- [2] F. Zhang, W. Chen, J. Lin, Z. Wang, Bidirectional linear ultrasonic motor using longitudinal vibrating transducers, *IEEE Trans. Ultrason. Ferroelectr. Freq. Control* 52 (1) (2005) 134–138, <http://dx.doi.org/10.1109/TUFFC.2005.1397358>.
- [3] K. Spanner, O. Vyshnevskyy, W. Wischnewskiy, New linear ultrasonic micromotor for precision mechatronic systems, *Proceedings of the 10th International Conference on New Actuators (Actuator 2006)* (2006) 439–443.
- [4] Y. Shi, C. Zhao, A new standing-wave-type linear ultrasonic motor based on in-plane modes, *Ultrasonics* 51 (4) (2011) 397–404, <http://dx.doi.org/10.1016/j.ultras.2010.11.006>.
- [5] Z. Wan, H. Hu, Modeling and experimental analysis of the linear ultrasonic motor with in-plane bending and longitudinal mode, *Ultrasonics* 54 (3) (2014) 921–928, <http://dx.doi.org/10.1016/j.ultras.2013.11.004>.
- [6] M. Guo, S. Pan, J. Hu, C. Zhao, S. Dong, A small linear ultrasonic motor utilizing longitudinal and bending modes of a piezoelectric tube, *IEEE Trans. Ultrason. Ferroelectr. Freq. Control* 61 (4) (2014) 705–709, <http://dx.doi.org/10.1109/TUFFC.2014.2958>.
- [7] T. Mashimo, S. Toyama, Rotary-linear piezoelectric actuator using a single stator, *IEEE Trans. Ultrason. Ferroelectr. Freq. Control* 56 (1) (2009) 114–120, <http://dx.doi.org/10.1109/TUFFC.2009.1010>.
- [8] T. Shigematsu, M.K. Kurosawa, K. Asai, Nanometer stepping drives of surface acoustic wave motor, *IEEE Trans. Ultrason. Ferroelectr. Freq. Control* 50 (4) (2003) 376–385, <http://dx.doi.org/10.1109/TUFFC.2003.1197960>.
- [9] M.K. Kurosawa, M. Chiba, T. Higuchi, Evaluation of a surface acoustic wave motor with a multi-contact-point slider, *Smart Mater. Struct.* 7 (3) (1998) 305, <http://dx.doi.org/10.1088/0964-1726/7/3/005>.
- [10] M.K. Kurosawa, H. Itoh, K. Asai, Elastic friction drive of surface acoustic wave motor, *Ultrasonics* 41 (4) (2003) 271–275, [http://dx.doi.org/10.1016/S0041-624X\(02\)00451-1](http://dx.doi.org/10.1016/S0041-624X(02)00451-1).
- [11] K. Asai, M.K. Kurosawa, T. Higuchi, Evaluation of the driving performance of a surface acoustic wave linear motor, in: *Ultrasonics Symposium, 2000, IEEE*, Vol. 1, IEEE, 2000, pp. 675–679, <http://dx.doi.org/10.1109/ULTSYM.2000.922638>.
- [12] I.A. Viktorov, *Rayleigh and Lamb Waves: Physical Theory and Applications*: Translated from Russian, Plenum press, 1967, pp. 1–7 (Chapter 1).
- [13] N. Garg, C.-S. Han, Axisymmetric couple stress elasticity and its finite element formulation with penalty terms, *Arch. Appl. Mech.* 85 (5) (2015) 587–600, <http://dx.doi.org/10.1007/s00419-014-0932-0>.
- [14] K. Asai, M.K. Kurosawa, Surface acoustic wave motor using an energy circulation driving method, in: *Ultrasonics Symposium, 2001 IEEE*, Vol. 1, IEEE, 2001, pp. 525–529, <http://dx.doi.org/10.1109/ULTSYM.2001.991677>.
- [15] M.M.P.A. Vermeulen, F.G.P. Peeters, H. Soemers, P.J. Feenstra, P.C. Breedveld, Development of a surface acoustic wave planar motor under closed loop control, *3rd EUSPEN International Conference, Eindhoven University of Technology* (2002) 107–110.

- [16] T. Shigematsu, M.K. Kurosawa, Friction drive modeling of saw motor using classical theory of contact mechanics, Proc. of 10th Conf. on New Actuators (2006) 444–448.
- [17] M.K. Kurosawa, T. Shigematsu, Friction drive simulation of a saw motor with slider surface texture variation, in: Advances in Science and Technology, Vol. 54, Trans. Tech. Publ., 2008, pp. 366–371, <http://dx.doi.org/10.4028/www.scientific.net/AST.54.366>.
- [18] M.K. Kurosawa, T. Shigematsu, Friction drive simulation of surface acoustic wave motor characteristics based on contact mechanics, Japan. J. Appl. Phys. 47 (5S) (2008) 4287, <http://dx.doi.org/10.1143/JJAP.47.4287>.
- [19] K.L. Johnson, Normal Contact of Elastic Solids – Hertz Theory, in: Contact Mechanics, 1985, Cambridge University Press, 1985, pp. 84–106 (Chapter 4).
- [20] T.R. Joseph, K.M. Lakin, Two-port cavity resonator low-insertion-loss delay line, Appl. Phys. Lett. 26 (7) (1975) 364–365, <http://dx.doi.org/10.1063/1.88180>.
- [21] C. Dagdeviren, P. Joe, O.L. Tuzman, K.-I. Park, K.J. Lee, Y. Shi, Y. Huang, J.A. Rogers, Recent progress in flexible and stretchable piezoelectric devices for mechanical energy harvesting, sensing and actuation, Extreme Mech. Lett. 9 (2016) 269–281, <http://dx.doi.org/10.1016/j.eml.2016.05.015>.
- [22] S. Gebhardt, L. Seffner, F. Schlenkrich, A. Schönecker, PZT thick films for sensor and actuator applications, J. Eur. Ceram. Soc. 27 (13) (2007) 4177–4180, <http://dx.doi.org/10.1016/j.jeurceramsoc.2007.02.122>.
- [23] A. Nagarajan, Ultrasonic study of elasticity–porosity relationship in polycrystalline alumina, J. Appl. Phys. 42 (10) (1971) 3693–3696, <http://dx.doi.org/10.1063/1.1659671>.

Biographies



Richard Günther received his M.Sc. (diploma) in Electrical Engineering from the Dresden University of Technology, Dresden, Germany, in 2009. Since 2009 he has worked as research associate and doctoral candidate at Dresden University of Technology. His main research interests are in the field of predevelopment of miniaturized actuators and medical devices. Since 2015 he took over lectureships in design fundamentals and numeric simulation at Bautzen University of Cooperative Education, Bautzen, Germany.



René Richter received the M.Sc. (diploma) in Electrical Engineering from the Dresden University of Technology, Dresden, Germany, in 2001. He joined the Hatfield Science and Technology Research Institute at the University of Hertfordshire, UK, with a research program focused on micro pumps. In the year 2002, he continued his research at Dresden University of Technology on micro pumps for drug delivery devices and received his Ph.D. in 2008. Currently, his main research interests are in the field of drug delivery devices, micro pumps and actuators.



Jens Lienig received his M.Sc. (diploma), Ph.D. (Dr.-Ing.) and Habilitation degrees in Electrical Engineering from Dresden University of Technology, Dresden, Germany, in 1988, 1991 and 1996, respectively. He is currently a Full Professor of Electrical Engineering at Dresden University of Technology (TU Dresden) where he is also Director of the Institute of Electromechanical and Electronic Design (IFTE). From 1999 to 2002, he worked as Tool Manager at Robert Bosch GmbH in Reutlingen, Germany, and from 1996 to 1999, he was with Tanner Research Inc. in Pasadena, CA. From 1994 to 1996, he was a Visiting Assistant Professor with the Department of Computer Science, University of Virginia, Charlottesville, VA, and from 1991 to 1994, a Postdoctoral Fellow at Concordia University in Montréal, QC, Canada. His current research interests are in physical design automation, with a special emphasis on electromigration avoidance, 3D design, and constraint-driven design methodologies of analog circuits. Professor Lienig has served on the Technical Program Committees of the DATE, SLIP and ISPD conferences. He is a Senior Member of IEEE.

Corrigendum by the authors, added October 21, 2019

We, the authors of this paper, claimed to provide “an extension of the theory of Rayleigh waves applied to cylindrical rods in axial direction of propagation, the resulting analytical quantification of these SAW and the analytical characterization of appropriate axisymmetric SAW motors.” After publication of this paper, we noticed that the first part of this claim (applying the theory of Rayleigh waves to cylindrical rods in axial direction of propagation) has been described in an earlier paper by Pochhammer in 1875 [24].

Despite missing the earlier work by Pochhammer, the other contributions of the published work, such as (1) the analytical characterization of appropriate axisymmetric SAW motors, (2) the working plane SAW motor with a stator made from non-piezoelectric material, and (3) the SAW generation on a plane non-piezoelectric material by an actuator unit which is made by use of thick-film technology, are presented for the first time.

We would like to apologize for any inconvenience caused.

[24] Pochhammer, L., “Ueber die Fortpflanzungsgeschwindigkeiten kleiner Schwingungen in einem unbegrenzten isotropen Kreiscylinder”, Journal für die reine und angewandte Mathematik, G. Reimer, Vol. 81, 324 – 336, 1875.

This is a personal version of this paper. The original version has been published by ScienceDirect with the DOI:

<https://doi.org/10.1016/j.sna.2019.04.024>

Please cite this paper as follows:

R. Günther, R. Richter, J. Lienig “Contributions to the Development of an Axisymmetric SAW Motor With a Stator Made from Non-Piezoelectric Material”, Sensors and Actuators A: Physical, vol. 295, pp. 274–287, ISSN 09244247, 15 Aug 2019